scientific reports

Check for updates

OPEN

A machine learning-based immune response signature to facilitate prognosis prediction in patients with endometrial cancer

Xiaofeng Wang[1,5], Jing Guan[2,5], Li Feng[3], Qingxue Li[3], Liwei Zhao[1], Yue Li[1], Ruixiao Ma[1], Mengnan Shi[1], Biaogang Han[1], Guorong Hao[3], Lina Wang[3], Hui Li[3]✉ & Xiuli Wang[4]✉

Endometrial cancer is the most prevalent form of gynecologic malignancy, with a significant surge in incidence among youngsters. Although the advent of the immunotherapy era has profoundly improved patient outcomes, not all patients benefit from immunotherapy; some patients experience hyperprogression while on immunotherapy. Hence, there is a pressing need to further delineate the distinct immune response profiles in patients with endometrial cancer to enhance prognosis prediction and facilitate the prediction of immunotherapeutic responses. The ssGSEA method was used to evaluate the activities of the immune response pathways in patients with endometrial cancer. Unsupervised clustering was employed to identify the different immune response patterns. WGCNA was employed to identify the genes that highly correlated with the immune response patterns observed. Ninety-five machine learning combinations were utilized to identify the optimal prognosis model and the novel biomarker, SLC38A3. Experiments such as cell invasion, migration, scratch, and in vivo tumorigenicity were performed to determine the function of SLC28A3. Molecular docking techniques were employed to determine the targeted action of periodate-oxidized adenosine on SLC38A3. Patients exhibited both immune response-suppressing C1 phenotypes and immune response-activating C2 phenotypes, with significant differences in prognosis between these two phenotypes. WGCNA identified 418 genes that highly correlated with the immune response phenotypes, of which 69 genes were associated with prognosis. The immune response-related score (IRRS) established by multiple machine learning frameworks demonstrated stability in predicting patient prognosis and immune status. High expression of SLC38A3 contributes to cellular malignant traits, and periodate-oxidized adenosine bound stably to SLC38A3. IRRS accurately predicts disease prognosis and immune status in patients with endometrial cancer. SLC38A3 serves as a prognostic marker for these patients and can be stably targeted by periodate-oxidized adenosine.

Keywords Endometrial cancer, Immune response, Machine learning, Prognosis, SLC38A3

Abbreviations

IRRS	Immune response-related score
UCEC	Uterine corpus endometrial carcinoma
NSMP	No specific molecular profile
EEC	Endometrioid endometrial cancer
ICI	Immune checkpoint inhibitors
WGCNA	Weighted gene co-expression network analysis
ssGSEA	Single sample gene set enrichment analysis
GO	Gene ontology
KEGG	Kyoto encyclopedia of genes and genomes
C-index	Concordance index

[1]Department of Oncology, The Fourth Hospital of Shijiazhuang, Shijiazhuang, Hebei Province, China. [2]Department of Radiology, The Fourth Hospital of Shijiazhuang, Shijiazhuang, Hebei Province, China. [3]The Fourth Hospital of Shijiazhuang, Shijiazhuang, Hebei Province, China. [4]Department of Laboratory Medicine, The Second Hospital of Hebei Medical University, Shijiazhuang, Hebei Province, China. [5]Xiaofeng Wang and Jing Guan contributed equally to this work. ✉email: lihuismile@126.com; 27700206@hebmu.edu.cn

CDF	Cumulative distribution function
PCA	Principal component analysis
UMAP	Uniform manifold approximation and projection
t-SNE	T-distributed stochastic neighbor embedding
ROC	Receiver operating characteristic
AUC	Area under the curve
RSF	Random survival forest
Enet	Elastic network
plsRcox	Partial least squares regression for Cox
SuperPC	Supervised principal components
GBM	Generalised boosted regression
Survival-SVM	Survival support vector machine
GSEA	Gene set enrichment analysis
TME	Tumor microenvironment
TAMs	Tumor-associated macrophages
TIDE	Tumor immune dysfunction and exclusion
OS	Overall survival
PFS	Progression-free survival
DSS	Disease-specific survival
DFS	Disease-free survival

Uterine corpus endometrial carcinoma (UCEC), the most prevalent form of gynecological malignancy[1], has seen a steady rise in incidence, with a noticeable surge particularly among younger populations. Currently, the primary treatment for UCEC includes surgical interventions such as hysterectomy, bilateral salpingo-oophorectomy, and pelvic lymph node dissection[2]. While effective, these procedures, especially hysterectomy, entail invasive measures that compromise the fertility of patients. Moreover, patients in the advanced stage of the disease have limited therapeutic options and their treatment outcomes remain suboptimal[3]. The pathogenesis of UCEC revolves around the excessive proliferation of the endometrial glands, resulting in an abnormal gland-to-stroma ratio[4,5]. The diagnosis and classification of UCEC primarily rely on the histological phenotypes of the tumor cells obtained through endometrial biopsy or curettage. The histological subtypes of UCEC include endometrioid, clear cell, serous, and mucinous carcinomas. Endometrioid endometrial cancer (EEC) is the most common subtype of UCEC, accounting for 75–90% of the cases[6]. EEC occurrence correlates closely with prolonged exposure to estrogen and typically presents with abnormal bleeding, an early sign of the disease that offers the most favorable prognosis[7]. Mucinous carcinoma contributes to approximately 10% of all UCEC cases, while clear cell and serous endometrial cancers are rare, collectively constituting less than 5% of all patients[7].

In UCEC, as in many cancers, the heterogeneity of the tumor immune microenvironment correlates with the immune responses[8]. This encompasses interactions between the tumor cells and the stroma, as well as interactions between the tumor cells and infiltrating immune cells[9]. Certain UCEC subtypes are characterized by significant immune cell infiltration, suggesting the potential efficacy of immunotherapy as an alternative or adjunct to surgery[10]. Consequently, research on the tumor immune microenvironment of UCEC primarily focuses on assessing the response pattern of specific UCEC subtypes to immunotherapy. Most of these studies are associated with immune checkpoint inhibitors (ICI). However, the success rates of ICI therapy are inconsistent, and the majority of the UCEC cases undergoing ICI treatment are still in clinical trial phases[11]. Exploring alternative approaches to immune modulation may expand the therapeutic spectrum, making the personalized treatment of UCEC more feasible[12].

To discover more effective immunotherapeutic options for endometrial cancer, we aimed to explore the immune landscape of UCEC and identify key molecular drivers associated with immune response modulation. Using unsupervised clustering algorithms and weighted gene co-expression network analysis (WGCNA), we sought to characterize distinct immune response phenotypes in UCEC and uncover novel therapeutic targets. Additionally, we integrated various machine learning frameworks to develop an immune response-related score (IRRS), which may offer predictive insights into patient immune responses and the immune microenvironment. These approaches aim to provide a foundation for developing more personalized and effective immunotherapy strategies for UCEC in the future.

Materials and methods

Data and data processing

The TCGAplot package of R (version 4.3.1) was utilized for the comprehensive analysis of the pan-cancer transcriptomic and clinical data obtained from the TCGA website[13]. Subsequently, the transcriptomic and clinical data of patients with uterine corpus endometrial carcinoma were extracted from the TCGAplot package and subjected to subsequent analysis. A single-sample gene set enrichment analysis (ssGSEA) algorithm was employed to explore the enrichment of the immune response-related gene sets within the UCEC samples. ssGSEA[14] is a computational methodology employed to assess gene set enrichment within individual samples, thus providing insights into the activity levels of the immune-related genes across diverse samples. The immune response-related gene sets utilized in this analysis were sourced from the Gene Ontology (GO) database. ssGSEA was performed utilizing the 'gsva()' function in the GSVA package of R, retaining the absolute ranking information (abs.ranking = TRUE). The method parameters were configured to "ssgsea", and Gaussian kernel density estimation (kcdf = "Gaussian") was employed for enrichment analysis. To normalize the ssGSEA results, the ssGSEA scores obtained were transformed to a range of 0–1, thereby facilitating enhanced visualization and comparison. Moreover, the estimate package was utilized to estimate the scores for the tumor

microenvironment. This process entailed sequential steps, including utilization of the "filterCommonGenes()" and "estimateScore()" functions to compute scores for the immune cell content, stromal cell content, and tumor purity. The "filterCommonGenes()" function aimed to sieve out a set of genes shared across various samples based on the input file provided, thus refining the gene set under scrutiny to help focus on the commonly shared genes. The "estimateScore()" function played a pivotal role in generating scores for the immune cell content, stromal cell content, and tumor purity. The scores derived from the "estimateScore()" function were output to a file ("estimateScore.gct"), which contained the scores for the immune cell content, stromal cell content, and tumor purity for each sample.

Unsupervised clustering

To unravel the intricacies in the immune response patterns of patients with UCEC, sample clustering was performed utilizing the ConsensusClusterPlus algorithm. This clustering approach relied on the immune cell enrichment scores obtained through ssGSEA. Specifically, the ConsensusClusterPlus package[15] in R was employed for sample clustering analysis. To explore the diverse clustering outcomes, the maximum number of clusters (K value) was varied from 1 to 9 with an interval of 1. To ensure robustness, the clustering analysis was performed for 1000 iterations. The parameter "pltem" served as a feature retention threshold, dictating the number of features (genes) retained for clustering analysis at each bootstrap iteration. In our settings, "pltem" was configured to 0.8, indicating that 80% of the features would be retained at each bootstrap iteration. Moreover, the parameter "pFeature" determined the probability of feature retention, with a value of 1 signifying the retention of every feature at each bootstrap iteration without feature selection. This setup was particularly suitable for scenarios involving the consideration of all features or when dealing with a relatively limited number of features. The clustering process was executed using the k-means clustering algorithm (clusterAlg = "km") and the Euclidean distance (distance = "Euclidean") was calculated. The clustering results were visualized using the ggplot2 package of R.

Survival analysis

Survival analysis was performed using the "survival" and "survminer" packages of R and Kaplan–Meier survival curves were constructed. We assessed four key endpoints: overall survival (OS), which represents the time from diagnosis to death from any cause; progression-free survival (PFS), indicating the time from diagnosis to either disease progression or death; disease-specific survival (DSS), defined as the time from diagnosis to death specifically caused by the disease (with non-disease-related deaths treated as censored data); and disease-free survival (DFS), which measures the time from initial treatment to either disease recurrence or death. We utilized the "survfit" function to compute Kaplan–Meier survival curves and employed the "survdiff" function to conduct log-rank tests for survival differences between expression groups. Censored cases, which included patients lost to follow-up or those alive without events at the end of the study, were managed by censoring at their last follow-up or event-free timepoint. Survival curves were visualized with the "ggsurvplot" function, providing clear depictions of survival differences between groups, with significance levels indicated by *P*-values (<0.05).

Enrichment analysis

We conducted enrichment analysis using the GSEABase, ClusterProfiler[16], and org.Hs.eg.db packages of R, in conjunction with the MetaScape website. The datasets utilized for enrichment analysis were derived from the Gene Ontology (GO)[17] and Kyoto Encyclopedia of Genes and Genomes (KEGG) databases. Enrichment analysis was executed employing the "EnrichGO" function, wherein pathways with a *P*-value <0.05 were deemed significantly enriched. Visualization of the results was accomplished using the "ggplot2" packages of R.

Construction of a prognostic model using machine learning

We utilized the machine learning survival framework established by Liu et al.[18], which is available at https://github.com/Zaoqu-Liu/IRLS, to implement our model. A total of 10 machine learning algorithms were implemented in R, namely random survival forest (RSF), elastic network (Enet), Lasso, Ridge, stepwise Cox, CoxBoost, partial least squares regression for Cox (plsRcox), supervised principal components (SuperPC), generalized boosted regression (GBM), and survival support vector machine (survival-SVM). One algorithm was utilized to filter the variables while another was employed to construct the prognostic signature. An important criterion for the prognostic signature was that, if the final prognostic signature contained fewer than two genes, it was deemed invalid. Subsequently, Harrell's concordance index (C-index) was computed for each prognostic signature. The signature exhibiting the highest average C-index was considered the best. Following the calculation of risk scores for each patient using the "predict" function, the optimal cutoff value for the risk score was determined using the "surv_cutpoint" function within the "survminer" package of R. Based on this optimal cutoff value, the patients were stratified into high- and low-risk groups.

mutation analysis

The mutation data for TCGA patients was retrieved from the cBioPortal database (https://www.cbioportal.org/datasets). To analyze differences in gene mutation frequencies between high-risk and low-risk patient groups, we used the mafCompare function from the maftools package. For visualization, the forestplot package was employed to create clear and interpretable plots of mutation frequency comparisons between the groups.

Pathway and immune function assessment

We applied the ssGSEA method to evaluate functional pathways and calculate immune cell infiltration scores. Hallmark gene set signatures were downloaded from the molecular signatures database (https://www.gsea-msig

db.org/gsea/msigdb/index.jsp), and immune cell-related signatures were obtained from the study by Pornpimol Charoentong et al.[19]. We also performed GSEA analysis for further validation, with all parameters set to default values. Tumor Immune Dysfunction and Exclusion (TIDE) analysis was conducted through the TIDE platform (http://tide.dfci.harvard.edu/). Additionally, immune therapy response scores for TCGA patients were accessed from the TCIA database (https://tcia.at/home)[20,21].

Cell culture and SLC38A3 knock-down

The ISHIKAWA cell line used in this study was obtained from the cell bank of the Fourth Hospital of Shijiazhuang City, Hebei Province, China. The cell was thawed and revived using standard procedures. The cells were cultured in RPMI1640 medium (Gibco, 11,875,093, USA) supplemented with 10% heat-inactivated fetal bovine serum (Gibco, A5670701, USA) at 37 °C in a 5% CO_2 incubator, with medium change every 2 days. Once the cells reached stable passages, the cells in the logarithmic phase of growth were selected for subsequent experiments. The cells in the knock-down group (sh-SLC38A3) were infected with lentiviral particles carrying shRNA (SLC38A3) sequences while those in the knock-down control group (sh-NC) were infected with slow viral particles carrying Scramble sequences. The sequence used for sh-SLC38A3 is 5′-AAACCCAGGGCTGCCTTGGAAAAG-3′. For the real-time RT-PCR assay, total RNA was extracted from ISHIKAWA cells following the instructions provided by the Trizol reagent kit (Invitrogen, no.15596026, USA, cat). cDNA synthesis was performed using the Takara Reverse Transcriptase cDNA Synthesis Kit (Takara, RR037A, Tokyo, Japan), and qRT-PCR was carried out using the Takara SYBR Green PCR Kit (Takara, RR820A, Tokyo, Japan). The sequences of primers for the SLC38A3 were as follows: forward: 5′-CCACCTGCTACTCAAGTCCTC-3′; reverse: 5′-GACATGGCTCCGATGTTCT GG-3′. Expression of GAPDH was performed as normalized. The sequences of primers for GAPDH were as follows: forward: 5′-CTGGGCTACACTGAGCACC-3′; reverse: 5′-AAGTGGTCGTTGAGGGCAATG-3′.

CCK-8 assay

For the CCK-8 assay, ISHIKAWA cells were seeded into 96-well plates at a density of 2×10^3 cells per well and incubated overnight to ensure adequate cell adherence. Afterward, 10 µL of the CCK-8 reagent (40203ES80, Yisean, Shanghai, China) was introduced into each well, followed by an additional 4-h incubation period. Optical density was measured at 450 nm using a microplate reader. Measurements were taken at 0, 24, 48, 72, and 96 h, with blank wells included as controls. Absorbance values were then used to plot a growth curve, enabling the assessment of ISHIKAWA cell proliferation over time.

Wound healing assay

Cell migration was evaluated using a wound healing assay following established protocols. ISHIKAWA cells that had been transfected were cultured in a 6-well plate until they reached 90% confluency. The cell monolayer was scratched using a micropipette to stimulate wounding and the cells were rinsed three times with sterile PBS to remove non-adherent cells. Subsequently, fresh serum-free culture medium was added to the wells, and the cells were further cultured. The wound status at both 0 and 24 h post-scratch was visualized using an X71 inverted microscope (Olympus), and the average distance between cells was calculated using the ImageJ software. All experiments were performed in triplicate to ensure statistical rigor.

Colony formation assay

ISHIKAWA cells were cultured under standard conditions in a 6-well plate. After a two-week incubation at 37 °C, the plate was washed with cold PBS to remove the non-adherent cells. Subsequently, the colonies were fixed using 4% paraformaldehyde for 15 min and stained with 0.1% crystal violet (Beyotime, C0121-500 ml, China) at room temperature. Imaging and quantification of the colonies were performed using a non-optical microscope.

Transwell assay

Cell migration was evaluated using Transwell assays following a 48-h. ISHIKAWA cells from each group were seeded into the upper chamber of Transwell inserts at a density of 4×10^4 cells/well in a medium containing 5% fetal bovine serum. Additionally, 500 µL of the medium was added to a 24-well culture plate in the lower chamber. After conventional culture for 24 h, the cells on the upper surface of the insert were removed using a cotton swab. Subsequently, the cells were fixed in a 4% paraformaldehyde solution for 10 min at room temperature and stained with a 0.5% crystal violet (Beyotime, C0121-500 ml, China) solution for 15 min. Finally, five randomly selected fields of view were examined under a light microscope to quantify the number of cells that had invaded the sub-layer membrane chamber.

In vivo mouse experiments

Female nude mice were purchased from GemPharmatech. The mice were randomly divided into groups, and a 1×10^7/150 µL cell suspension of Ishikawa-shNC (WT) or Ishikawa-shSLC38A3 (KD) cells were implanted into the right scapulas of the nude mice. After 11 days of inoculation, the mice were sacrificed, and the tumor was removed, weighed and measured. This project was supervised and approved by the Ethics Committee of the Fourth Hospital of Shijiazhuang City, Hebei Province, China, approval No. 20240064.

Molecular docking

The purpose of molecular docking is to predict the binding mode and affinity between a ligand molecule, in this case periodate-oxidized adenosine, and its target protein SLC38A3, thereby aiding in understanding their interaction at the molecular level. To achieve this goal, several steps were taken to ensure accuracy and reliability. Specifically, the 3D structure of periodate-oxidized adenosine was first obtained from the CTD database (https://

ctdbase.org/detail.go?type=chem&acc=C027579) and refined using the MM2 force field within the chemBio3D tool. This process involved energy minimization and optimization to obtain a stable and realistic representation of the ligand's conformation. The protein structure data of SLC38A3 was sourced from the AlphaFold Protein Structure database (https://alphafold.ebi.ac.uk/entry/Q99624). The protein structure was saved in PDB format and subjected to necessary refinement or preprocessing steps, such as removing water molecules or adding missing atoms. Molecular docking simulations were conducted using the AutoDock Vina program. This software employs a scoring algorithm to predict the binding affinity and orientation of the ligand within the protein's binding site. Through optimization of various parameters, AutoDock Vina efficiently explores the conformational space and identifies potential binding modes between the ligand and the protein. The scoring algorithm implemented in AutoDock Vina estimates the binding energy of the protein–ligand complex. This energy calculation serves as a quantitative measure of the strength of interaction between the ligand and the protein, with lower energy values indicating higher binding affinity. Finally, the results of molecular docking simulations were visualized and analyzed using PyMOL software. PyMOL facilitates the generation of high-quality molecular graphics, allowing for the depiction of ligand binding within the protein's active site. This visualization method aids in understanding the molecular interactions driving ligand–protein binding and helps identify key residues involved in ligand recognition and binding. By adopting this approach, we ensure the systematic execution of molecular docking. Each stage of the process is carefully designed to enhance the reliability and accuracy of the results, ultimately contributing to a deeper understanding of ligand–protein interactions.

Statistical analysis

All statistical analyses were performed using R, with the corresponding statistical methods set up in the R software. Statistical significance was set at $P < 0.05$. The significance levels were denoted as follows: $^{*}p < 0.05$, $^{**}p < 0.01$, and $^{***}p < 0.001$.

Results

Development and validation of immune response phenotypes in patients with endometrial cancer

All immune response-related pathways were retrieved from the Gene Ontology database. Subsequently, the ssGSEA method was employed and the pathway activity scores were obtained for all the immune response-related pathways in patients with endometrial cancer. Based on these pathway activity scores, unsupervised clustering was performed on all patients by initially dividing them into k (2–9) clusters. The cumulative distribution function (CDF) curves of the consensus score matrix revealed optimal clustering at K = 2 (Figure S1A–B, Fig. 1A). Moreover, Principal Component Analysis (PCA) (Fig. 1B), Uniform Manifold Approximation and Projection (UMAP) analysis (Figure S1C), and t-distributed Stochastic Neighbor Embedding (tSNE) analysis (Figure S1D) were performed utilizing the activity scores of these immune response pathways to reduce the dimensionality for all patients. The results demonstrated clear differentiation between the two clusters across the different dimensionality reduction methods, underscoring the robustness of our classification. Heatmaps depicting the pathway activity scores for the two clusters (Fig. 1C) revealed that the patients in Cluster 1 (C1) exhibited an immune response suppression phenotype while those in Cluster 2 (C2) displayed an immune response activation phenotype. Furthermore, the immune scores, stromal scores, ESTIMATE scores, and tumor purity were evaluated for all patients utilizing the "estimate" package (Fig. 1D). The findings revealed that the patients in C2 possessed significantly higher immune scores, stromal scores, and ESTIMATE scores, and lower tumor purity, compared to those in C1, suggesting that the patients in C2 had a propensity towards a hot tumor phenotype. Importantly, Kaplan–Meier analysis revealed a markedly better prognosis for the patients in the C2 cluster compared to those in the C1 cluster (Figure S1E), thus underscoring the prognostic predictive capability of the C2 immune response phenotype.

Identification of the immune response phenotype-associated genes

WGCNA was used to identify the genes that highly correlated with the two immune response phenotypes. The soft-thresholding power was set to 10 (Fig. 2A) as it yielded an appropriate power value for constructing a co-expression network. In total, 10 gene modules, each denoted by a distinct color, were identified (Fig. 2B). We assessed the correlation between each gene module and the clusters and found that the light green module exhibited the highest correlation (correlation coefficient = 0.63) (Fig. 2C). The light green module comprised 418 genes, and KEGG analysis (Fig. 2D) revealed that these genes were significantly enriched in the immune-related pathways such as cytokine-cytokine receptor interaction, Th17 cell differentiation, chemokine signaling pathway, Th1 and Th2 cell differentiation, natural killer cell-mediated cytotoxicity, and antigen processing and presentation. Additionally, GO enrichment analysis (Fig. 2E) highlighted the significant enrichment of the genes in pathways including leukocyte activation, regulation of cell activation, positive regulation of immune response, adaptive immune response, and inflammatory response. In summary, we identified 418 genes that are highly correlated with the immune response phenotypes.

Development of the optimal immune response-related prognostic features using a multi-machine learning survival framework

Before the construction of a prognostic model, a univariate Cox regression analysis was performed on the set of 418 genes, which helped identify 69 prognosis-related genes that correlated with the overall survival time and status (Figure S2A). Remarkably, all these genes demonstrated a protective effect ($HR < 1, p < 0.05$). Subsequently, all patients in the TCGA dataset were randomly partitioned into two groups at a ratio of 6:4 to establish train and test sets (Table S1). The set of 69 prognosis-related genes was then subjected to a multi-machine learning

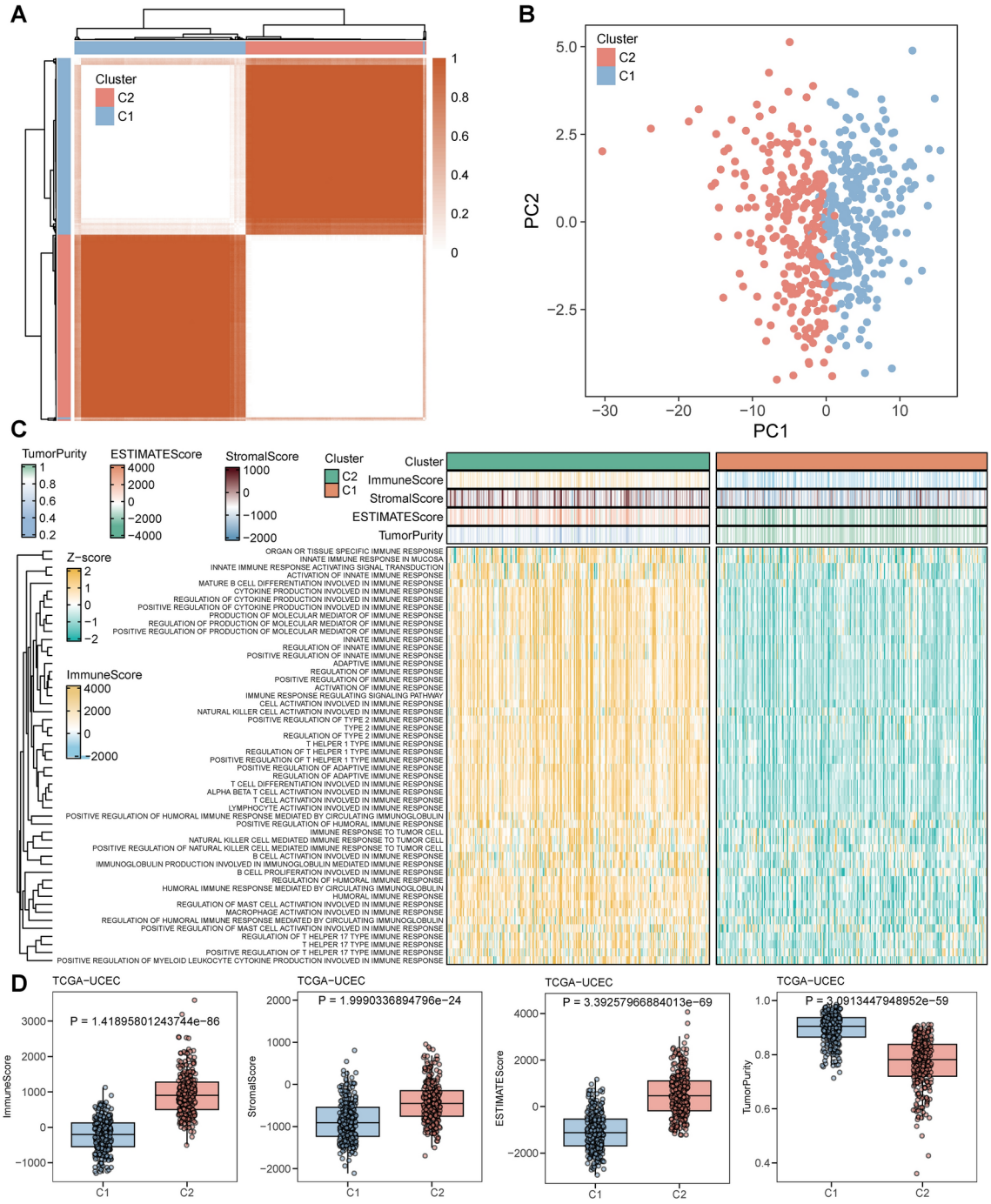

Fig. 1. Development and validation of immune response phenotypes in patients with endometrial cancer. (**A**) The correlation among patients when K = 2. Red represents high correlation, while white represents low correlation. (**B**) PCA analysis of patients based on their immune response pathway scores. C1 and C2 are clearly distinguished. (**C**) Heatmap representing the immune response pathway activity scores of patients across the two clusters. The more yellow the color, the higher the score; the more blue the color, the lower the score. (**D**) Immune scores, stromal scores, ESTIMATE scores, and tumor purity of the tumors in patients across the two clusters.

integration framework. The prognostic model was trained with the train set and subsequently validated with the test set. Ten distinct machine learning algorithms, namely RSF, Enet, Lasso, Ridge, stepwise Cox, CoxBoost, plsRcox, SuperPC, GBM, and survival-SVM were employed within this framework. Additionally, combinatorial analysis was applied to these machine learning algorithms. Specifically, the first algorithm was utilized for gene selection, while the second was employed for building the prognostic model. Throughout this process, to ensure robustness across the other cohorts, the prognostic model was deemed ineffective if it comprised fewer than

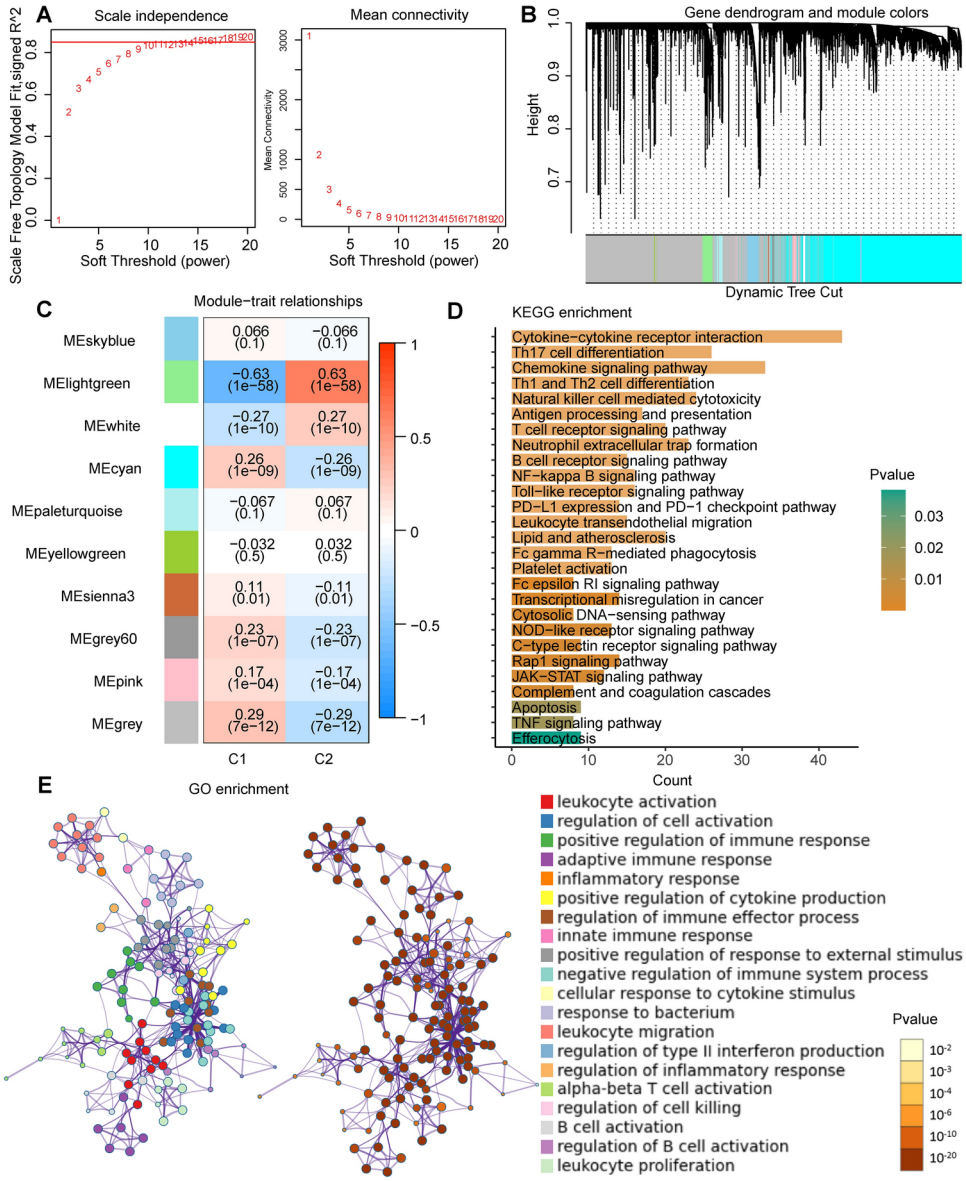

Fig. 2. Identification of the immune response phenotype-associated genes. (**A**) Determination of the soft threshold of WGCNA. R^2 changes with different soft thresholds; a relatively flat R^2 corresponds to an appropriate soft threshold for WGCNA analysis. The chosen soft threshold here is 10. (**B**) Identification of gene clustering modules. Different colors represent different gene modules. The waterfall plot shows clustering similarity between different modules. (**C**) Correlation analysis between gene modules and phenotypes, with the light green modules exhibiting a high level of correlation with the clusters. (**D**) KEGG enrichment analysis. The more yellow the color, the lower the *p*-value; the more green the color, the higher the *p*-value. (**E**) GO enrichment analysis. For terms, different colored points represent different biological functions. For *p*-values, redder colors indicate greater significance.

two genes. Consequently, a total of 95 prognostic models were constructed, and the C-index was computed for each gene signature (Fig. 3A). Ranking of the C-index values of the test sets revealed that the LASSO + RSF model combination had the highest C-index value of 0.6942 (Fig. 3A). This outcome underscores the superior robustness and generalizability of this model combination, designating it as the best immune response-related model. Comprising 6 genes, the LASSO algorithm facilitated the selection of genes (LTB, GPR18, BATF, ACAP1, GRAP2, and CTSW) (Fig. 3B–C) while the RSF algorithm calculated the importance of each gene (Fig. 3D). Moreover, an immune response-related score (IRRS) was generated for each patient based on these 6 genes. The optimal IRRS cutoff value for patient stratification was determined using the "survminer" package (Figure S2B). We observed that, with increasing IRRS, the number of deceased patients gradually increased and the expression levels of the 6 genes gradually decreased in both the train and test sets (Fig. 3E–F). Receiver operating characteristic (ROC) curve analysis further demonstrated the high predictive accuracy of the train cohort, with an area under the curve (AUC) of 0.99, 0.98, and 0.998, at 1, 3, and 5 years, respectively (Fig. 3G). Whilst there

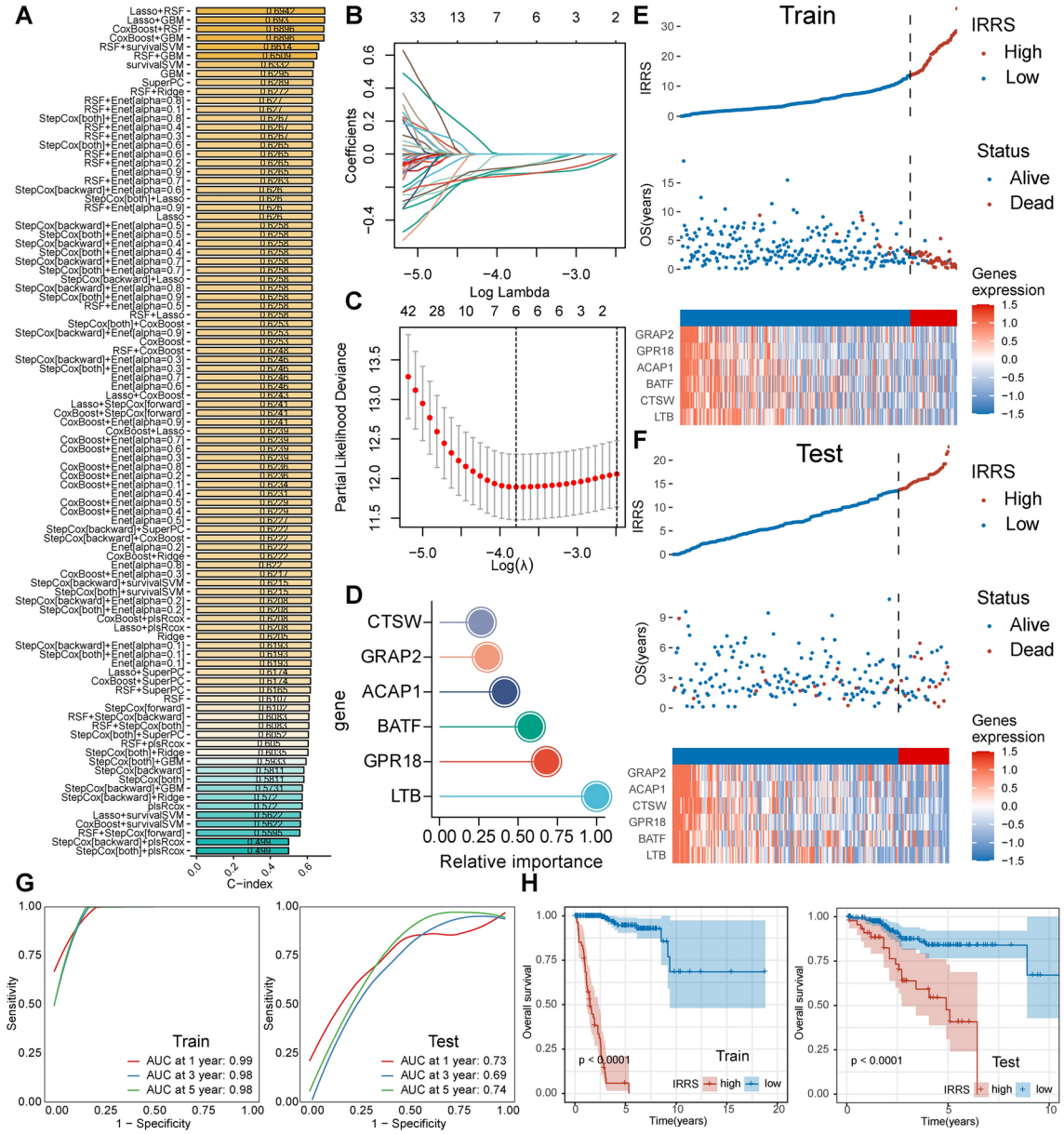

Fig. 3. Identification of the optimal immune response-related prognostic features using a multi-machine learning survival framework. (**A**) Representation of 95 prognostic models integrated through machine learning, along with their corresponding C-index values in the test cohort. All models are sorted in descending order by C-index from the test cohort. (**B**) LASSO coefficient path plot. This plot shows the coefficient paths of the variables as the regularization parameter (lambda) changes. Each colored line represents the trajectory of a variable's coefficient as it is penalized through the LASSO algorithm. The x-axis indicates the log-transformed lambda values, while the y-axis represents the coefficient values. As lambda increases (moving rightward), more variables' coefficients shrink toward zero, indicating feature selection. (**C**) LASSO cross-validation plot. This plot shows the cross-validation results for the LASSO Cox regression model. The y-axis represents the partial likelihood deviance, quantifying the model's goodness-of-fit to the survival data. The x-axis represents the log of the regularization parameter (lambda). The dotted vertical line indicates the lambda value that results in the minimum deviance, while the second dotted line shows the largest lambda value within one standard error of the minimum deviance (optimal for model simplicity). (**D**) RSF analysis for computing the importance of each gene. This plot illustrates the importance of each gene as determined by the RSF model. The y-axis represents the genes analyzed in the model, and the x-axis shows the variable importance score, indicating each gene's contribution to the survival prediction. Higher scores suggest greater influence on the model's prediction accuracy. The importance score is computed based on the change in prediction error when a gene's value is randomly permuted while other genes remain unchanged. (**E**–**F**) Distribution of gene expression and patient survival status based on IRRS in the train and test cohorts. Higher risk scores correlate with more deaths and lower expression of the six genes. (**G**) ROC analysis of patients with high and low IRRS in different cohorts. (**H**) Overall survival analysis of patients with high and low IRRS in different cohorts.

may be overfitting of this, it is crucial to note that the AUC values in the test cohort were 0.73, 0.69, and 0.74, at 1, 3, and 5 years, respectively (Fig. 3G). Survival analysis revealed a significant reduction in the overall survival among patients in the high-IRRS group compared to those in the low-IRRS group, in both the train and test datasets (Fig. 3H). In summary, the development of IRRS underscores its robust effectiveness, stability, and reliability.

Immunodeficiency and low-frequency mutations in patients with a high IRRS favor immune escape from tumors

We examined the association between IRRS and the functional characteristics of patients. First, we found that higher IRRS scores were associated with greater suppression of immune response pathways in patients (Fig. 4A). Patients with a high IRRS exhibited significantly lower immune scores, stromal scores, and ESTIMATES scores, and higher tumor purity, compared to those with a low IRRS (Figure S3A). Furthermore, GSEA analysis (Fig. 4B) revealed that patients with a high IRRS presented with significant suppression of various immune-related pathways such as adaptive immune response, cell killing, neutrophil migration, and positive regulation of T-cell activation. Moreover, ssGSEA, which was used to assess the infiltration of multiple immune cell types in patients, revealed a significant negative correlation between IRRS and all immune cell types (Fig. 4C). Additionally, evaluation of the changes in the effector pathways of patients revealed a positive correlation between IRRS and the activity of pathways like G2M checkpoint, mitochondrial division, and E2F targets, and a negative correlation between IRRS and the TNFA signaling pathway, IL6-JAK-STAT3 signaling pathway, and p53-mediated cell apoptosis pathway (Fig. 4C). According to the existing immune subtype classification from TCGA, we found that the C4 subtype (Lymphocyte Depleted) had the highest risk score, followed by the C1 (Wound Healing), C3 (Inflammatory), and C2 (IFN-gamma Dominant) subtypes, consistent with our research findings (Fig. 4D). Subsequently, the Tumor Immune Dysfunction and Exclusion (TIDE) algorithm was employed to assess patient immune treatment response levels, and the results revealed significantly higher TIDE scores among patients with high IRRS compared to those with low IRRS (Fig. 4E), with non-responders to immune therapy possessing a higher IRRS than responders (Fig. 4F). The TCIA algorithm was used to further validate these results by analyzing patient response to anti-CTLA4 and anti-PD1 treatments. The findings revealed that patients with low IRRS were more likely to benefit from both single and combined treatments with anti-CTLA4 and anti-PD1 (Fig. 4G, Figure S3B). Analysis of the potential relationship between IRRS and gene mutations revealed a significantly lower mutation rate in patients with high IRRS compared to those with low IRRS (Fig. 4C-D), suggesting a more stable genome in the patients with high IRRS. Finally, after comparing the relationship between the high IRRS and low IRRS groups with the four established subtypes[22] of endometrial carcinoma, we found that in the high IRRS group, the proportion of the CN high subtype increased, while the proportion of the POLE subtype decreased (Figure S3E). In summary, our findings suggest that patients with high IRRS are characterized by immune system dysfunction and significantly reduced immune cell infiltration, which predisposes them to cold tumors. Additionally, low-frequency mutations in patients with high IRRS might facilitate the ability of tumor cells to evade the immune microenvironment.

The IRRS-based identification of SLC38A3 promotes the malignant capability of tumor cells

To further explore the potential performance of IRRS, a differential analysis was conducted between patients with high IRRS and those with low IRRS (Fig. 5A). We found that the genes that promote T cell cytotoxicity, such as LTB, CD3E, CD3D, and NKG7, were significantly downregulated in patients with high IRRS, which is consistent with our research findings (Fig. 5A). Among the upregulated genes, we found that the solute carrier family 38, member 3 (SLC38A3) gene had the largest -log10 FDR value (Fig. 5A). We classified all patients into a high SLC38A3 expression group and a low SLC38A3 expression group based on the optimal cutoff value, using a combination of survival data and SLC38A3 expression levels. Importantly, we found that patients with high levels of SLC38A3 expression had worse prognosis in terms of OS, PFS, DSS, and DFS than those with low levels of SLC38A3 expression (Fig. 5B), indicating that SLC38A3 can serve as a prognostic marker. In the TCGA database, we found that the SLC38A3 expression levels correlated with the Grade grading and Stage staging of patients with endometrial cancer (Fig. 5C). To explore the effect of SLC38A3 on tumor cell proliferation, migration, invasion, and in vivo growth, an endometrial cancer cell line with SLC38A3 knock-down, ISHIKAWA, was constructed. Real-time RT-PCR assay in the ISHIKAWA cell line showed that the expression level of SLC38A3 in the sh-SLC38A3 group was significantly lower than that in the sh-NC group (Fig. 5D). CCK-8 experiments in the ISHIKAWA cell line showed that the proliferation ability of the cells in the sh-SLC38A3 group was significantly lower than that of the cells in the sh-NC group (Fig. 5E). Colony formation experiments in the ISHIKAWA cell line showed that the colony formation ability of the cells in the sh-SLC38A3 group was significantly lower than that of the cells in the sh-NC group (Figure S4A-B), suggesting that SLC38A3 knock-down can inhibit the proliferation ability of ISHIKAWA cells. Moreover, the migration rate of the cells in the sh-SLC38A3 group was significantly lower than that of the cells in the sh-NC group in the ISHIKAWA cell line (Fig. 5F-G). Invasion experiments showed that the number of cells passing through the transwell chamber in the sh-SLC38A3 group was significantly lower than that in the sh-NC group (Fig. 5H-I). These results suggest that SLC38A3 knock-down can inhibit the invasion ability of the ISHIKAWA cells. The scratch test results showed that SLC38A3 knock-down can reduce the area of wound healing in 24 h, indicating reductions in cell proliferation and migration in SLC38A3 knock-down ISHIKAWA cell (Fig. 5J, Figure S4C). The ISHIKAWA cell line was used to construct a subcutaneous tumor model in nude mice, and this subcutaneous tumor was dissected to demonstrate that the volume of the subcutaneous tumor in the sh-SLC38A3 group was smaller than that in the sh-NC group (Fig. 5K). Quantitative analysis of the tumor volume revealed that the volume of the subcutaneous tumor in the sh-SLC38A3 group was significantly smaller than that in the sh-NC group, right from the eighth day after the subcutaneous implantation of the tumor cells in nude mice (Figure S4D). In

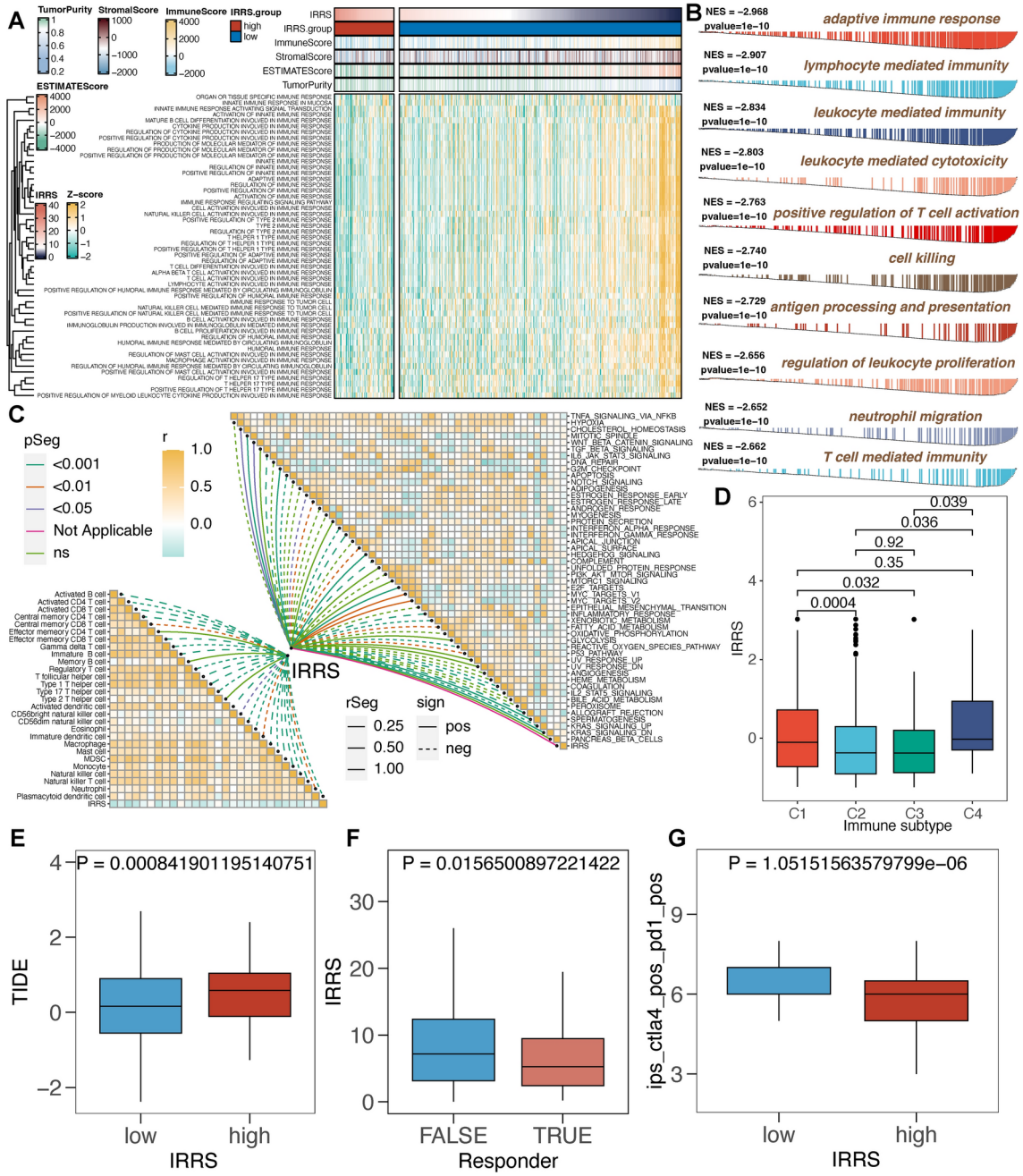

Fig. 4. Immunodeficiency and low-frequency mutations in patients with high IRRS favor immune escape from tumors. (**A**) Heatmap depicting the gradual decrease in immune response pathway activity scores with increasing IRRS. (**B**) GSEA showing multiple suppressed immune and cytotoxic pathways in patients with high IRRS. An NES value greater than 0 indicates pathway activation, while an NES value less than 0 indicates pathway suppression. (**C**) Correlation heatmap illustrating the relationship between IRRS and various immune cell infiltrations and effector pathways. (**D**) Boxplot showing differences in IRRS among different immune subtypes in datasets derived from TCGA. Immune subtypes are based on the study by Vésteinn Thorsson et al.[59]. C1 is Wound Healing, C2 is IFN-gamma Dominant, C3 is Inflammatory, and C4 is Lymphocyte Depleted. (**E**) Comparison of TIDE scores between patients with high and low IRRS, where higher TIDE scores indicate greater potential for immune escape. (**F**) Differences in IRRS between immune therapy responders and non-responders. (**G**) Sensitivity of anti-CTLA4 combined with anti-PD-1 therapy in patients with high and low IRRS.

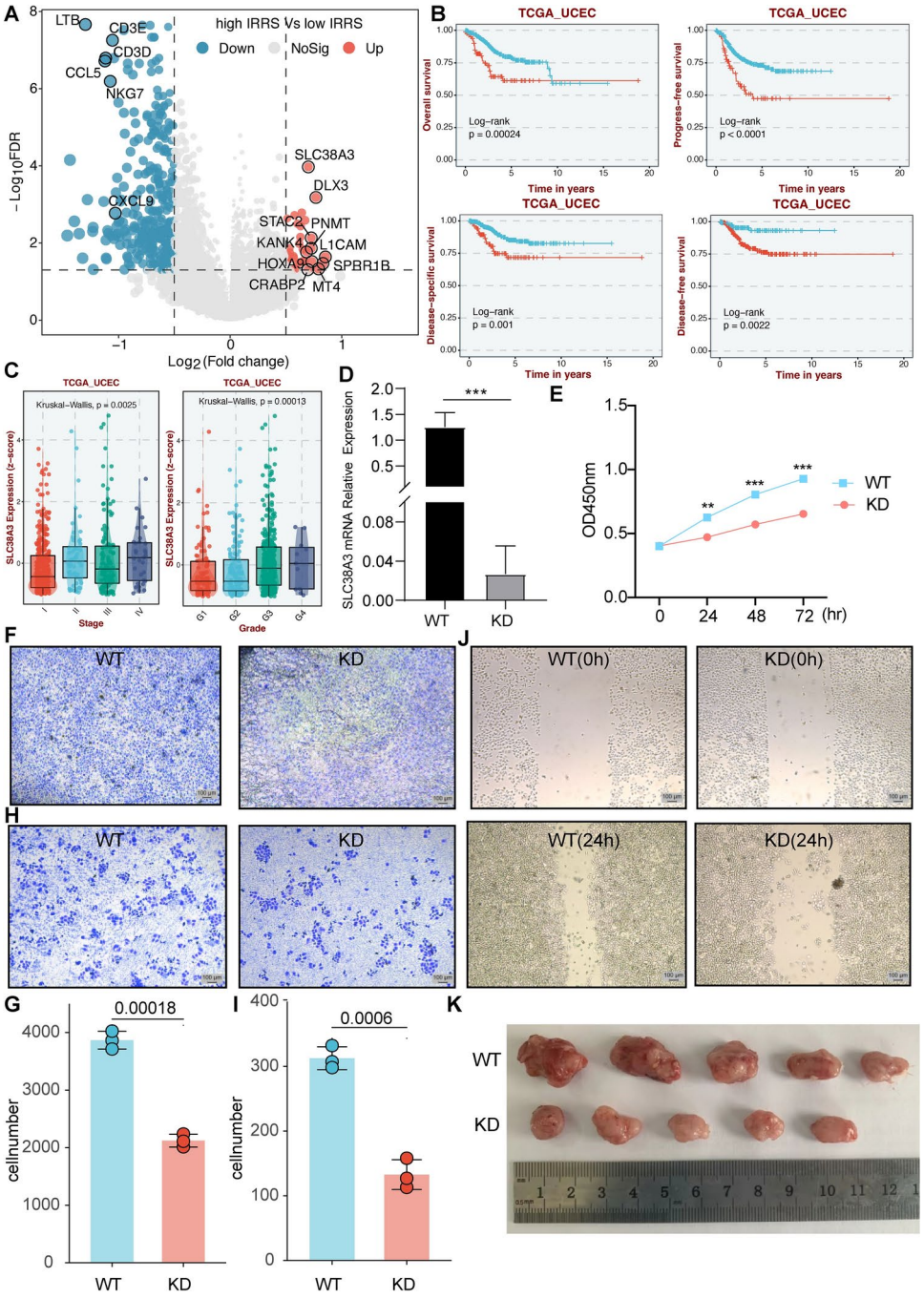

Fig. 5. IRRS-based identification of SLC38A3 promotes the malignant capability of tumor cells. (**A**) Differential analysis between patients with high and low IRRS. (**B**) Survival analysis of SLC38A3 across different survival indicators, with high and low SLC38A3 groups defined by the optimal cutoff value. (**C**) Expression levels of SLC38A3 in different stages and grades of endometrial cancer (EC). (**D**) Gene expression levels of SLC38A3 in knockdown (KD) and wild-type (WT) models. (**E**) OD450nm values from CCK-8 experiments in KD and WT models. (**F**) Number of migratory cells in KD and WT models. (**G**) Statistical quantification of the migratory cells. (**H**) Number of invading cells in WT and KD models. (**I**) Statistical quantification of the invading cells. (**J**) Wound healing rate at 24 h in WT and KD models. (**K**) Tumor size measurements in WT and KD models. The significance levels are represented by asterisks as follows: $*p < 0.05$, $**p < 0.01$, $***p < 0.001$. Asterisks indicate statistically significant differences between groups, with increasing significance denoted by more asterisks.

summary, the knock-down of the expression of SLC38A3 leads to slower growth of the ISHIKAWA cells in nude mice, smaller tumor volumes, and lower tumor burden in nude mice.

Periodate-oxidized adenosine is a stable binder of SLC38A3

To further enhance the clinical translation of our research findings, we utilized the Enrichr database (https://maayanlab.cloud/Enrichr/) to predict small molecule drugs capable of targeting SLC38A3. A total of 9 different small molecule drugs were identified, among which 3 drugs (Periodate-oxidized adenosine, 3′-Azido-3′-deoxythymidine, carbamazepine) emerged as statistically significant ($P < 0.05$) (Table 1). Periodate-oxidized adenosine was a significantly enriched drug, with an odds ratio of 19,784 and a combined score of 89,586.28316. To characterize the main functions of periodate-oxidized adenosine, a GO enrichment analysis was conducted of all of its target genes (https://ctdbase.org/detail.go;jsessionid=2499E0250571AB190A80086CCDCF1C2D?type=chem&acc=C027579&view=gene) (Fig. 6A). The findings revealed significant impacts on metabolism (fatty acid metabolism, amino acid metabolism), immune response, and TP53 signaling, all of which are closely associated with the function of SLC38A3. Furthermore, to validate the stability of periodate-oxidized adenosine targeting SLC38A3, molecular docking was performed using computational simulation techniques. Our findings revealed that periodate-oxidized adenosine bound stably within the protein pocket of SLC38A3 with an affinity of -5.9 kcal/mol. It formed hydrogen bonds with the LYS-165 (2.5 Å), TYR-162 (3.2 Å), PRO-426 (3.6 Å), ASN-427 (3.1 Å, 2.3 Å), and SER-350 (3.4 Å) residues of the SLC38A3 protein (Fig. 6B). In conclusion, our results indicate that periodate-oxidized adenosine effectively targets SLC38A3 with high stability and specificity.

Discussion

While approximately 80% of endometrial cancers can be diagnosed in the early stage of disease and these patients present with a five-year survival rate exceeding 95%, patients with advanced or recurrent disease face poor prognosis owing to the low efficacy of standard chemotherapy[1]. Immunotherapy has emerged as an effective treatment option for solid tumors such as endometrial cancer[23]. Several clinical trials have investigated the efficacy and safety of the programmed cell death protein 1 (PD-1) antibody, pembrolizumab, a checkpoint inhibitor, in endometrial cancer, and obtained promising results[24–26]. To further enhance the treatment efficacy, numerous studies are currently exploring the effectiveness of combining checkpoint inhibitors with chemotherapy, radiotherapy, and other targeted therapies[27]. Additionally, further research is needed to unveil novel specific biomarkers that accurately predict immunotherapy response. For this, first, we scored the immune response pathways in all patients with endometrial cancer and classified them into two categories (C1 and C2). Patients in the C1 group exhibited an immune response-inhibited phenotype while those in the C2 group showed an immune response-activated phenotype. This finding aligns with that in previous reports, suggesting a correlation between endometrial cancer heterogeneity and its immune microenvironment. The quantity of tumor-infiltrating immune cells (TIICs) in endometrial cancer correlates with the differences in prognosis, thereby highlighting the relevance of the tumor microenvironment (TME) in endometrial cancer diagnosis and treatment. $CD8^+$ T-cell infiltration typically signifies a favorable prognosis[28–30]. However, late-stage endometrial cancer is characterized by a low T-cell density[31,32]. Indeed, low copy number endometrial cancers have the second-highest mortality rate[33]. Previous studies have investigated the correlation between the molecular subtypes and the tumor-infiltrating immune cell density and phenotype and found a high proportion of $CD8^+$ T-cells in the POLEmut and MMRd tumors, most of which express immune checkpoint molecules, particularly programmed cell death protein 1 (PD-1)[34]. A high level of PD-1 expression in tumor-infiltrating T-cells serves as a target for immune checkpoint inhibitors[35]. Effective PD-1 inhibition can prevent PD-L1 binding, thereby improving immune tolerance via the PD-1/PD-L1 pathway and enhancing T-cell efficacy[36]. Therefore, patients in the C2 group are more likely to benefit from anti-PD-1 therapies.

A total of 418 genes that highly correlated with the immune response phenotype were selected using WGCNA. Of these, 69 genes were associated with prognosis. A multi-machine learning integration framework was used and six key genes (LTB, GPR18, BATF, ACAP1, GRAP2, and CTSW) were selected to construct an immune response prognosis prediction model. We found that the patients with validated high-IRRS endometrial cancer presented with immune function suppression, a reduction in the levels of tumor-infiltrating immune cells (characteristic of cold tumors), and low responsiveness to immunotherapy. Additionally, these patients also exhibited genomic stability, which favors immune escape. Tumor-infiltrating immune cells have been identified as prognostic

Genes	Drugs	*P*-value	Odds ratio	Combined score
SLC38A3	periodate-oxidized adenosine	0.010799894	19,784	89,586.28316
SLC38A3	3′-Azido-3′-deoxythymidine	0.018699859	19,626	78,096.55061
SLC38A3	carbamazepine	0.021799848	19,564	74,848.97418
SLC38A3	AFLATOXIN B1	0.154049743	16,919	31,646.64642
SLC38A3	quercetin	0.157899743	16,842	31,086.87909
SLC38A3	estradiol	0.216799758	15,664	23,946.82753
SLC38A3	benzo[a]pyrene	0.22119976	15,576	23,499.34134
SLC38A3	cyclosporin A	0.241249767	15,175	21,577.67398
SLC38A3	copper sulfate	0.300799793	13,984	16,799.12428

Table 1. Drug enrichment analysis of SLC38A3.

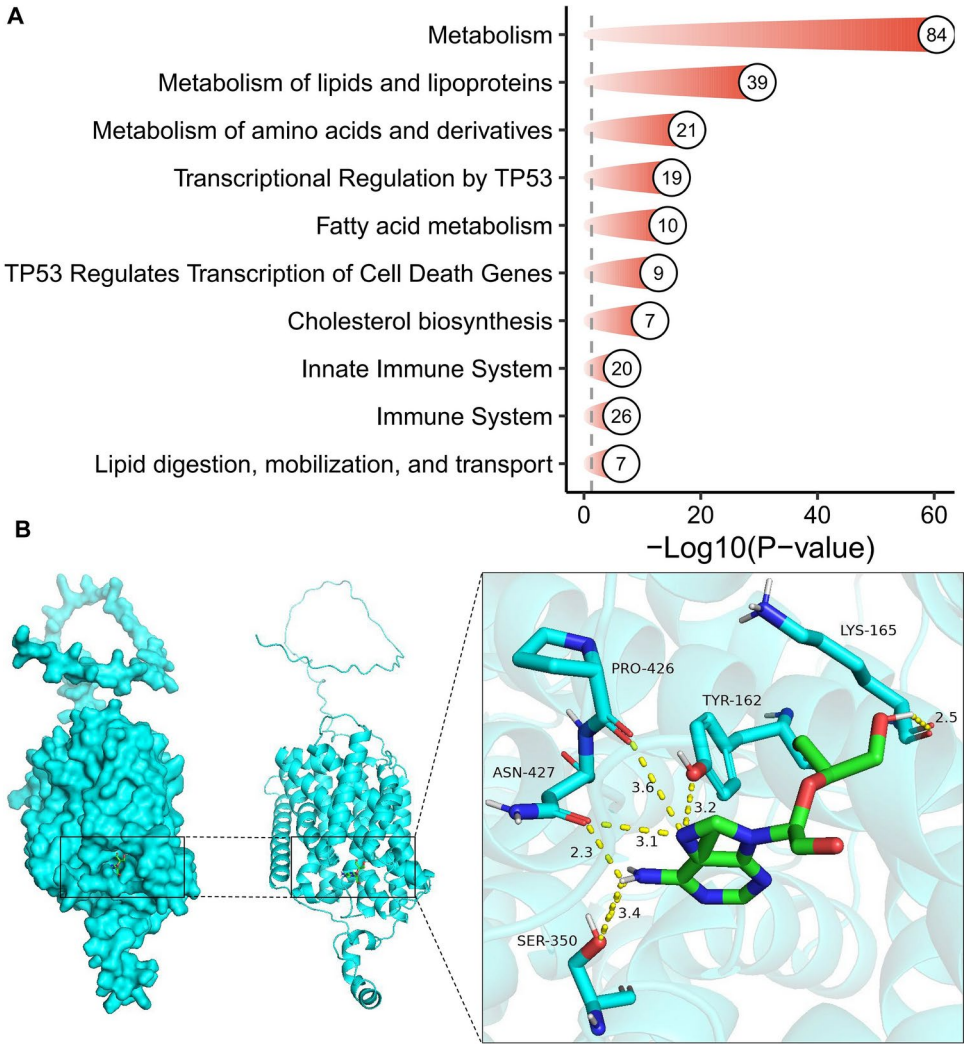

Fig. 6. Periodate-oxidized adenosine as a stable binder of SLC38A3. (**A**) Gene Ontology (GO) enrichment analysis of all targets of periodate-oxidized adenosine. (**B**) Molecular docking representation illustrating the interaction between periodate-oxidized adenosine and SLC38A3, with yellow dashed lines indicating hydrogen bond interactions.

indicators in various cancers (melanoma, endometrial cancer, ovarian cancer, and colorectal cancer)[37–39], and positively correlate with the severity of UCEC[8]. However, the relationship between specific immune subgroups and their prognostic prediction ability remains unclear. For instance, a certain amount of regulatory T-cells (Tregs) positively correlates with overall survival in No Specific Molecular Profile (NSMP)[40] but negatively correlates with overall survival in p53abn UCEC[8], suggesting the specific role of this molecular subtype of T-cells in prognostic prediction. Besides significant levels of T-cell infiltration, UCEC also exhibits a significant increase in the level of CD3-CD56^{+} NK cells in the tumor tissue compared to the non-tumor tissue[41]. It remains unclear, however, whether these cells are depleted as a result of tumor signals or other pathways. But the most likely result of this depletion is tumor immunotolerance. Besides T cells, tumor-associated macrophages (TAMs) also constitute a diverse subset of tumor-infiltrating immune cells. TAMs are derived from monocytes and possess traditional cytotoxic[42] and phagocytic characteristics[43]. However, they are associated with cancer tolerance. An increase in the TAM counts has been observed in the tumor and stromal tissues of patients with UCEC compared to the benign pathological controls[44]. However, TAM density shows no significant correlation with cancer progression. Thus, the clinical or prognostic significance of measuring TAM density in UCEC remains unclear. Further studies have found an increase in the macrophage density in the stromal interstitium with increasing disease severity, with fewer macrophages in the proliferative phase of endometrial hyperplasia, and the highest macrophage density in non-endometrioid UCEC, which tends to be more aggressive[45]. However, the histology of different forms of UCEC has revealed that the cell density of TAMs expressing the M2 macrophage marker CD163 remains similar across the different forms of UCEC[45], suggesting that the infiltrating TAMs in the more aggressive forms of UCEC primarily consist of pro-inflammatory M1-like subtypes. Conversely, co-culturing tumor cell-derived exosomes with monocyte-derived macrophages induces an M2-like phenotype in the macrophages[46], indicating that tumor cells can polarize macrophages toward immune tolerance. While

there is some evidence on the state and function of TAMs in UCEC, further research is needed. In addition to measuring the quantity of the effector cells, it is also important to consider the impact of the regulatory immune cell subsets (such as Tregs and myeloid-derived suppressor cells) on effector cell function. Combining functional markers and regulatory immune subsets with immune cell density can provide a more accurate understanding of the interactions within the tumor microenvironment, enabling researchers to develop specific tools targeting the factors conducive to cancer progression.

Utilizing IRRS, for the first time, we have reported the role of SLC38A3 in the immune microenvironment of endometrial cancer. SLC38A3 knock-down affects the proliferation, migration, and invasion capabilities of endometrial cancer cells both in vitro and in vivo. This marks the initial report of the involvement of SLC38A3 in endometrial cancer. SLC38A3, a member of the solute carrier family, serves as a sodium-dependent amino acid transporter primarily facilitating the transport of non-essential amino acids like glutamate and aspartate[47]. SLC38A3 brings about the transport of these amino acids from the extracellular to the intracellular space by co-transporting them with sodium ions. This functionality is crucial for cellular metabolism, nutrient absorption, and neurotransmitter balance[48]. SLC38A3 is expressed in various tissues, including the liver, brain, and muscles[48]. In the brain, it likely contributes to the regulation of glutamate levels, a major excitatory neurotransmitter, while in the liver, it likely participates in amino acid metabolism and release, which are essential for systemic amino acid balance and protein synthesis[49]. The role of SLC38A3 in the onset and progression of endometrial cancer, however, has not been studied extensively or reported. In oncology, the heightened cellular demand for nutrients, especially those essential for supporting rapid proliferation[50], underscores the potential significance of the expression and activity of amino acid transporters in cancer development[51]. Based on our research findings, we hypothesize that SLC38A3 may facilitate tumor cell growth and survival by modulating intra- and extra-cellular amino acid concentrations, thereby potentially promoting the proliferation and viability of the tumor cells[52]. Additionally, cancer cells often reprogram their metabolic pathways to sustain rapid growth[53], and SLC38A3 may participate in regulating these pathways, particularly in amino acid metabolism.

SLC38A3 may influence the tumor microenvironment and affect tumor immune evasion by modulating the metabolism of immune cells. For instance, LTB, a chemokine for lymphocytes[54], may have its expression and function impacted by amino acid levels within tumor cells. Tumor cells can alter the availability of amino acids to modify LTB expression, thereby affecting lymphocyte migration and activation. The expression of GPR18 in immune cells is closely related to immune responses[55]. If tumor cells elevate the concentration of certain amino acids through SLC38A3 regulation, this may inhibit GPR18 activity and weaken the efficacy of immune cells. BATF, as a transcription factor, plays a crucial role in the differentiation of T cells and B cells[56,57]. SLC38A3 may regulate the mTOR signaling pathway by influencing amino acid uptake and metabolism in tumor cells, which in turn affects BATF expression and function[58]. This interaction could lead to changes in the dynamic balance between tumor cells and immune cells, ultimately impacting immune responses. Additionally, ACAP1 and GRAP2 are important in intracellular signaling pathways. The expression of SLC38A3 may alter the interactions between tumor cells and immune cells, regulating the activity of ACAP1 and GRAP2 and influencing cell migration, proliferation, and apoptosis. Although our study represents the first documentation of the role of SLC38A3 in endometrial cancer, the specific mechanisms involved require further exploration. Furthermore, the sensitivity and resistance of cells to chemotherapy drugs may be associated with their amino acid uptake and utilization, which could also be influenced by SLC38A3. Furthermore, through computational simulation techniques, we have identified that periodate-oxidized adenosine is capable of stably binding to SLC38A3, thus supporting its clinical translation.

In summary, we have developed a robust IRRS and identified the correlation between patients with high IRRS and immune response inhibition and cold tumor characteristics. IRRS enables the prediction of patient prognosis. Knock-down experiments of the key gene, SLC38A3, have confirmed its role in regulating tumor behavior, offering new directions for treatment. However, our study has some limitations. The sample size was small due to the limited availability of endometrial cancer cohorts. Therefore, further validation of the findings utilizing IRRS is needed in larger cohorts. Additionally, the role and drug optimization of periodate-oxidized adenosine targeting SLC38A3 requires further exploration.

Data availability

All data are available in the main Excel or the supplementary materials. Transcriptomic and clinical data for all patients were obtained from TCGA databases (https://portal.gdc.cancer.gov/). The code can be accessed at https://www.jianguoyun.com/p/Dcb_B5QQ5478DBiE7OUFIAA. All models can be obtained from https://www.jianguoyun.com/p/DQYGdK4Q5478DBiZ7eUFIAA.

Received: 19 March 2024; Accepted: 25 November 2024
Published online: 28 December 2024

References

1. Sung, H. et al. Global cancer statistics 2020: GLOBOCAN Estimates of incidence and mortality Worldwide for 36 cancers in 185 Countries. *CA Cancer J. Clin.* **71**, 209–249 (2021).
2. Braun, M. M., Overbeek-Wager, E. A. & Grumbo, R. J. Diagnosis and management of endometrial cancer. *Am. Fam. Physician* **93**, 468–474 (2016).
3. Janda, M. et al. Complete pathological response following levonorgestrel intrauterine device in clinically stage 1 endometrial adenocarcinoma: Results of a randomized clinical trial. *Gynecol. Oncol.* **161**, 143–151 (2021).
4. Crosbie, E. J. et al. Endometrial cancer. *Lancet* **399**, 1412–1428 (2022).
5. Nees, L. K. et al. Endometrial hyperplasia as a risk factor of endometrial cancer. *Arch. Gynecol. Obstet.* **306**, 407–421 (2022).

6. Rabban, J. T. et al. Issues in the differential diagnosis of uterine low-grade endometrioid carcinoma, including mixed endometrial carcinomas: Recommendations from the International Society of Gynecological Pathologists. *Int. J. Gynecol. Pathol.* **38**, S25–S39 (2019).
7. Bell, D. W. & Ellenson, L. H. Molecular genetics of endometrial carcinoma. *Annu. Rev. Pathol. Mech. Dis.* **14**, 339–367 (2019).
8. Willvonseder, B. et al. The immunologic tumor microenvironment in endometrioid endometrial cancer in the morphomolecular context: Mutual correlations and prognostic impact depending on molecular alterations. *Cancer Immunol. Immunother.* **70**, 1679–1689 (2021).
9. Mahdi, H., Chelariu-Raicu, A. & Slomovitz, B. M. Immunotherapy in endometrial cancer. *Int. J. Gynecol. Cancer* **33**, 351–357 (2023).
10. Marín-Jiménez, J. A., García-Mulero, S., Matías-Guiu, X. & Piulats, J. M. Facts and hopes in immunotherapy of endometrial cancer. *Clin. Cancer Res.* **28**, 4849–4860 (2022).
11. Cao, W. et al. Immunotherapy in endometrial cancer: rationale, practice and perspectives. *Biomark. Res.* **9**, 49 (2021).
12. Di Tucci, C. et al. Immunotherapy in endometrial cancer: new scenarios on the horizon. *J. Gynecol. Oncol.* **30**, e46 (2019).
13. Liao, C. & Wang, X. TCGAplot: an R package for integrative pan-cancer analysis and visualization of TCGA multi-omics data. *BMC Bioinform.* **24**, 483 (2023).
14. Barbie, D. A. et al. Systematic RNA interference reveals that oncogenic KRAS-driven cancers require TBK1. *Nature* **462**, 108–112 (2009).
15. Wilkerson, M. D. & Hayes, D. N. ConsensusClusterPlus: A class discovery tool with confidence assessments and item tracking. *Bioinformatics* **26**, 1572–1573 (2010).
16. Wu, T. et al. clusterProfiler 4.0: A universal enrichment tool for interpreting omics data. *Innovation* **2**, 100141 (2021).
17. Ashburner, M. et al. Gene ontology: Tool for the unification of biology. *Nat. Genet.* **25**, 25–29 (2000).
18. Liu, Z. et al. Machine learning-based integration develops an immune-derived lncRNA signature for improving outcomes in colorectal cancer. *Nat. Commun.* **13**, 816 (2022).
19. Charoentong, P. et al. Pan-cancer immunogenomic analyses reveal genotype-immunophenotype relationships and predictors of response to checkpoint blockade. *Cell Rep.* **18**, 248–262 (2017).
20. Van Allen, E. M. et al. Genomic correlates of response to CTLA-4 blockade in metastatic melanoma. *Science* **350**, 207–211 (2015).
21. Hugo, W. et al. Genomic and transcriptomic features of response to Anti-PD-1 therapy in metastatic melanoma. *Cell* **165**, 35–44 (2016).
22. Cancer Genome Atlas Research Network et al. Integrated genomic characterization of endometrial carcinoma. *Nature* **497**, 67–73 (2013).
23. Tronconi, F. et al. Advanced and recurrent endometrial cancer: State of the art and future perspectives. *Crit. Rev. Oncol. Hematol.* **180**, 103851 (2022).
24. Mamat Yusof, M. N., Chew, K. T., Kampan, N. C. & Shafiee, M. N. Expression of PD-1 and PD-L1 in endometrial cancer: Molecular and clinical significance. *Int. J. Mol. Sci.* **24**, 15233 (2023).
25. Johnson, R. L. et al. Immune checkpoint inhibitors targeting the PD-1/PD-L1 pathway in advanced, recurrent endometrial cancer: A scoping review with SWOT analysis. *Cancers (Basel)* **15**, 4632 (2023).
26. Mamat Yusof, M. N. et al. Efficacy and safety of PD-1/PD-L1 inhibitor as single-agent immunotherapy in endometrial cancer: A systematic review and meta-analysis. *Cancers (Basel)* **15**, 4032 (2023).
27. Karpel, H., Slomovitz, B., Coleman, R. L. & Pothuri, B. Biomarker-driven therapy in endometrial cancer. *Int. J. Gynecol. Cancer* **33**, 343–350 (2023).
28. De Jong, R. A. et al. Presence of tumor-infiltrating lymphocytes is an independent prognostic factor in type I and II endometrial cancer. *Gynecol. Oncol.* **114**, 105–110 (2009).
29. Kondratiev, S., Sabo, E., Yakirevich, E., Lavie, O. & Resnick, M. B. Intratumoral CD8+ T lymphocytes as a prognostic factor of survival in endometrial carcinoma. *Clin. Cancer Res.* **10**, 4450–4456 (2004).
30. Workel, H. H. et al. CD103 defines intraepithelial CD8+ PD1+ tumour-infiltrating lymphocytes of prognostic significance in endometrial adenocarcinoma. *Eur. J. Cancer* **60**, 1–11 (2016).
31. Čermáková, P. et al. Prognostic significance of CD3+ tumor-infiltrating lymphocytes in patients with endometrial carcinoma. *Anticancer Res.* **34**, 5555–5561 (2014).
32. Fusco, M. J., West, H. & Walko, C. M. Tumor mutation burden and cancer treatment. *JAMA Oncol.* **7**, 316 (2021).
33. Talhouk, A. et al. Confirmation of ProMisE: A simple, genomics-based clinical classifier for endometrial cancer. *Cancer* **123**, 802–813 (2017).
34. Talhouk, A. et al. Molecular subtype not immune response drives outcomes in endometrial carcinoma. *Clin. Cancer Res.* **25**, 2537–2548 (2019).
35. Dong, H. & Chen, L. B7–H1 pathway and its role in the evasion of tumor immunity. *J. Mol. Med.* **81**, 281–287 (2003).
36. Keir, M. E., Butte, M. J., Freeman, G. J. & Sharpe, A. H. PD-1 and its ligands in tolerance and immunity. *Annu. Rev. Immunol.* **26**, 677–704 (2008).
37. Ye, L. et al. Tumor-infiltrating immune cells act as a marker for prognosis in colorectal cancer. *Front. Immunol.* **10**, 2368 (2019).
38. Zhang, L. et al. Intratumoral T cells, recurrence, and survival in epithelial ovarian cancer. *N. Engl. J. Med.* **348**, 203–213 (2003).
39. Clemente, C. G. et al. Prognostic value of tumor infiltrating lymphocytes in the vertical growth phase of primary cutaneous melanoma. *Cancer* **77**, 1303–1310 (1996).
40. Chen, B., Wang, D., Li, J., Hou, Y. & Qiao, C. Screening and identification of prognostic tumor-infiltrating immune cells and genes of endometrioid endometrial adenocarcinoma: Based on the cancer genome atlas database and bioinformatics. *Front. Oncol.* **10**, 554214 (2020).
41. Degos, C. et al. Endometrial tumor microenvironment alters human NK cell recruitment, and resident NK cell phenotype and function. *Front. Immunol.* **10**, 877 (2019).
42. Qian, B.-Z. & Pollard, J. W. Macrophage diversity enhances tumor progression and metastasis. *Cell* **141**, 39–51 (2010).
43. Lin, Y., Xu, J. & Lan, H. Tumor-associated macrophages in tumor metastasis: Biological roles and clinical therapeutic applications. *J. Hematol. Oncol.* **12**, 76 (2019).
44. Dun, E. C. et al. Infiltration of tumor-associated macrophages is increased in the epithelial and stromal compartments of endometrial carcinomas. *Int. J. Gynecol. Pathol.* **32**, 576–584 (2013).
45. Kelly, M. G. et al. Type 2 endometrial cancer is associated with a high density of tumor-associated macrophages in the stromal compartment. *Reprod. Sci.* **22**, 948–953 (2015).
46. Xiao, L., He, Y., Peng, F., Yang, J. & Yuan, C. Endometrial cancer cells promote M2-like macrophage polarization by delivering exosomal miRNA-21 under hypoxia condition. *J. Immunol. Res.* **2020**, 1–9 (2020).
47. Rubio-Aliaga, I. & Wagner, C. A. Regulation and function of the SLC38A3/SNAT3 glutamine transporter. *Channels (Austin)* **10**, 440–452 (2016).
48. Chan, K. et al. Loss of function mutation of the Slc38a3 glutamine transporter reveals its critical role for amino acid metabolism in the liver, brain, and kidney. *Pflugers Arch.* **468**, 213–227 (2016).
49. Hamdani, E. H. et al. Perturbation of astroglial Slc38 glutamine transporters by NH4+ contributes to neurophysiologic manifestations in acute liver failure. *FASEB J.* **35**, e21588 (2021).
50. Tan, Z., Boyapati, K., Tressler, C. M., Jenkinson, N. & Glunde, K. Glutamine transporter SLC38A3 promotes breast cancer metastasis via Gsk3β/β-catenin/EMT pathway. *Cancer Lett.* **586**, 216653 (2024).

51. Liu, R. et al. Defect of SLC38A3 promotes epithelial-mesenchymal transition and predicts poor prognosis in esophageal squamous cell carcinoma. *Chin. J. Cancer Res.* **32**, 547–563 (2020).
52. Kholodnyuk, I. D. et al. Down regulation of 3p genes, LTF, SLC38A3 and DRR1, upon growth of human chromosome 3-mouse fibrosarcoma hybrids in severe combined immunodeficiency mice. *Int. J. Cancer* **119**, 99–107 (2006).
53. Wang, Y. et al. Amino acid transporter SLC38A3 promotes metastasis of non-small cell lung cancer cells by activating PDK1. *Cancer Lett.* **393**, 8–15 (2017).
54. Browning, J. L. et al. Lymphotoxin beta, a novel member of the TNF family that forms a heteromeric complex with lymphotoxin on the cell surface. *Cell* **72**, 847–856 (1993).
55. Mahardhika, A. B. et al. Potent, selective agonists for the cannabinoid-like orphan G protein-coupled receptor GPR18: A promising drug target for cancer and immunity. *J. Med. Chem.* **67**, 9896–9926 (2024).
56. Itahashi, K. et al. BATF epigenetically and transcriptionally controls the activation program of regulatory T cells in human tumors. *Sci. Immunol.* **7**, eabk0957 (2022).
57. Zhang, X. et al. Depletion of BATF in CAR-T cells enhances antitumor activity by inducing resistance against exhaustion and formation of central memory cells. *Cancer Cell* **40**, 1407-1422.e7 (2022).
58. Shin, B. et al. Mitochondrial oxidative phosphorylation regulates the fate decision between pathogenic Th17 and regulatory T cells. *Cell Rep.* **30**, 1898-1909.e4 (2020).
59. Thorsson, V. et al. The immune landscape of cancer. *Immunity* **48**, 812-830.e14 (2018).

Author contributions

Xiaofeng Wang, Jing Guan, Hui Li and Xiuli Wang conceived and wrote the paper. Xiaofeng Wang, Li Feng, Qingxue Li, Liwei Zhao, Yue Li, Ruixiao Ma, Mengnan Shi, Biaogang Han, Hui Li, Guorong Hao, Lina Wang, Jing Guan and Xiuli Wang analyzed the materials and drafted the manuscript. Xiaofeng Wang, Jing Guan, Hui Li and Xiuli Wang revised the whole paper. All authors have reviewed the final version of the manuscript and approved to submit to your journal.

Funding

All authors disclosed no relevant relationships.

Declarations

Competing interests

The authors declare no competing interests.

Ethics approval and consent to participate

All methods were carried out in accordance with relevant guidelines and regulations. The study is reported in accordance with ARRIVE guidelines. This project was supervised and approved by the Ethics Committee of the Fourth Hospital of Shijiazhuang City, Hebei Province, China, approval No. 20240064.

Consent for publication

All authors have agreed to publish this manuscript.

Additional information

Supplementary Information The online version contains supplementary material available at https://doi.org/10.1038/s41598-024-81040-7.

Correspondence and requests for materials should be addressed to H.L. or X.W.